7

Aerodynamic and Aeroacoustic Study of a High Rotational Speed Centrifugal Fan

Sofiane Khelladi, Christophe Sarraf, Farid Bakir and Robert Rey
DynFluid Lab., Arts et Métiers ParisTech
France

1. Introduction

In this chapter we propose a complete, numerical and experimental, analysis of aerodynamics and aeroacoustics of a high rotational speed centrifugal fan. The proposed approach can be extended to any subsonic turbomachine. The main objective of this chapter is to present the state of the art of conducting numerical simulations to predict the aerodynamic and the resulted acoustics of subsonic fans. Different approaches will be discussed and commented.

In our case, we will focus our study on a high rotational speed centrifugal fan, see figure (1). The numerical simulation of aerodynamics is performed using a URANS approach. The numerical results are validated experimentally before using them to supply the aeroacoustic model using a hybrid approach. For the aeroacoustic analysis, first, we will present and use the aeroacoustic analogy based on Ffowcs Williams and Hawkings (FW&H) formalism. And then we will present another advanced approach based on Linearised Euler Equations in which we will take into account reflections as well as rotating sources given by CFD.

2. Aerodynamic study

A shrouded centrifugal fan with high rotational speed and compact dimensions is studied in this paper. A review made by Krain (2005) clarified the state-of-the-arts of the potential development in the field of this kind of centrifugal turbomachinery. The review points out that many machines of moderate efficiency are still in operation but could certainly be improved by making use of recent knowledge in design and computation techniques. Shrouded impellers usually used in high-specific-speed-type centrifugal fans are linked downstream to a vaned diffuser, cross-over bend and return channel. In this type of machine there exists an unavoidable open cavity between the shrouded impeller and the outer casing. The cavity connects the oulet to the inlet of the impeller throught an axial gap and have , then, a significant influence on the performance of the machine.

Concerning the effects of impeller-diffuser interaction on the flow fields and the performance, several studies of this kind of turbomachinery are repported in litterature. It is shown that there always exist flow separations near the diffuser hub which extend further downstream, see Meakhail (2005) works. The flow is strongly three-dimensional with secondary flows on the hub and the shroud of the de-swirl vanes and significant separation occur downstream the cross-over bend, see Khelladi et al. (2005a;b). Consequently the flow is not really axisymmetric and the axial length of the cross-over bend must be increased of nearly 50% to compensate boundary layer blockage. However, there are significant disagreements between computed

and measured flow characteristics across the bend. For small sized compressor impellers, the leakage flow becomes major source of performance and efficiency drop as shown by Eum & Kang (2002). Thus, the way to control the leakage flow tends to become of major interest according to Ishida & Surana (2005).

The advanced CFD tools allow now the full optimization of centrifugal fan design, see Kim & Seo (2004); Schleer & Hong (2004); Zangeneh & Schleer (2004) works. For example, a three-dimensional unsteady viscous flow solution was numerically obtained by Khelladi et al. (2005a) by means of powerful computational facilities and robust software, although with very consumptive calculation time. Despite the knowledge accumulated over the past few decades on the design of turbomachinery, the accurate prediction of this kind of flow fields by numerical means is still difficult. This is partly due to the limits of the turbulent models and to the complexity of the flow through such a machine where occur separations and possibly non-axisymmetry having an effect on the performance of the components downstream, see Moon et al. (2003); Seo et al. (2003). There are still significant differences between computations and experimental results, mainly in the prediction of the separation after the bend and its extent.

As far as it concern recent design improvement, a criterion to define cross-flow fan design parameters is reported by Lazzaretto (2003) taking into account the most significant geometric variables affecting performance and efficiency. Other indications are found to design fans according to maximum total pressure criterion, total efficiency, and flow rate, see Lazzaretto et al. (2003); Toffolo (2004). The energy loss process was studied by Toffolo (2004) who compares theory and experiment results concerning performance and efficiency of centrifugal fans. Anyway, the mechanisms and the range of loss generation of centrifugal fans are not documented enough yet.

In this paper, a motor-fan of the kind used a vacuum cleaners was adopted for the study. The centrifugal fan features is characterised by its high specific speed, compact size with a throttling cavity, of interest, between the shrouded impeller and the outer casing. The major flow features in each component have been numerically investigated with a particular attention paid on the cavity. A second series of numerical simulations has been done with a model without cavity to estimate by comparison the effect of the latest. Further more, a basic volumetric loss model was coupled to the numerical model to obtain a cost effective solution. The results are compared with full numerical and experimental results. Finally, a new empirical constant accounting for the effect of the cavity is presented in the last section.

2.1 Numerical approach and experimental setup

2.1.1 Physical model

The motor-fan studied was used to provide large depression capability as required by a vacuum cleaner. The flow downstream is used to cool the motor but due to its complex internal geometry, it is difficult to simulate the flow field combined with the real motor components. Therefore, some assumptions are necessary. Apart from the investigation of flow around the motor structure, the flow through the fan itself is the main concern of research. As shown in figure (1), the studied centrifugal fan consists on the following components: centrifugal impeller with shrouded blades, diffuser and return channel. A diffuser with 17 vanes and a return channel with 8 irregular guide vanes de-swirls the flow. An upstream and downstream ducts are added to the numerical model. In order to better understand the effect of the cavity on the overall performance and the flow structure, a computational model

without cavity was configured (Case I), while for the real prototype at practical operating condition, there always exists a clearance between the rotating shrouded impeller and the stationary outer casing (Case II). Geometrical and operating parameters of the centrifugal fan are listed in Tables 1 and 2.

Head, H (m); ΔP(Pa)	1300; 0.159 10^5
Flow rate, Qv (m^3/s)	35×10^{-3}
Rotational speed, N (rpm)	34000
Specific speed $N_s = N\sqrt{Q_v}/H^{3/4}$	29

Table 1. Aerodynamic characteristics at operating point

Description	**Impeller**	**Diffuser**	**Return channel**
Radius of blade inlet (mm)	18	52.7	60
Span of the blade at the entry (mm)	13	6.48	11
Inlet blade angle (°)	64	85	74
Inclination Angle of the blade inlet (°)	85.8	0	0
Radius of blade exit (mm)	52	66.1	33
Span of the blade at the exit (mm)	5.4	8.43	12
Angle of blade exit (°)	64	71.6	15
Inclination angle of the blade exit (°)	0	0	0
Blade number	9	17	8
Blade thickness (mm)	0.8	0.9	1.6

Table 2. Basic geometrical specifications of the centrifugal fan

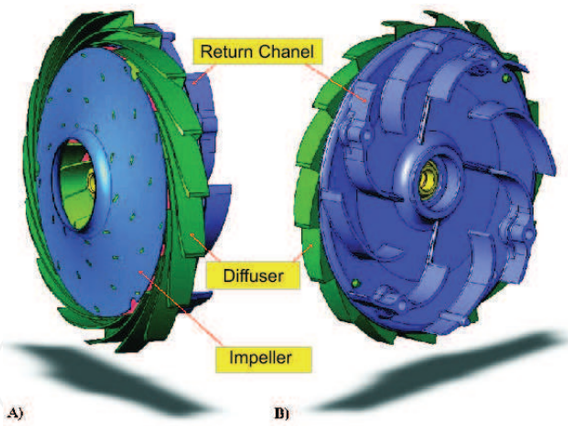

Fig. 1. Description of centrifugal fan system, A) front view, B) back view

2.2 Numerical model

The numerical simulations have been carried out with a code that is based on the finite volume method using FLUENT (1998) to solve the full 3D Reynolds Average Navier-Stokes equations. A centered SIMPLE algorithm is used for the pressure-velocity coupling and a second-order upwind scheme is used for the convection and diffusion terms. The unsteady equations are solved using an implicit second-order upwind scheme. The velocity is specified at the inlet surface for the inlet duct volume and the static pressure is imposed at the exit surface for the outlet duct. Nevertheless, the guide vanes in the return channel are featured as circumferential

asymmetry as shown in figure 1. Obviously, to control sound and vibration levels, the number of impeller blades and the number of diffuser vanes have no common divisor. Therefore, for an unsteady solution, the computational domain must cover all the fluid domain. In order to better approximate the near-wall viscous characteristics, the $k-\omega$ SST (Shear Stress Transport) model was adopted. The model treatment close to the wall combines a correction for high and low Reynolds number to predict separation on smooth surfaces, see Menter (1993) paper. Typically, this model gives a realistic estimation of the generation of the turbulent kinetic energy at the stagnation points. The SST model performance has been studied in a large number of cases. The model was rated the most accurate for aerodynamic applications in the NASA Technical Memorandum written by Bardina et al. (1997). As the geometry of the fan is complex, a hybrid mesh is used, composed of tetrahedral elements for the impeller, the diffuser and return channel volumes, and composed of hexahedral elements for upstream and downstream volumes of fluid. A previous study of Khelladi et al. (2005a) shows that a grid of 4.4×10^6 meshes is considered to be sufficiently reliable to make the numerical modeling results independent of the mesh size.

2.3 Measurement methodology

Measurements were carried out on a test bench (see figure 2) equipped with an airtight box (0.6 x 0.6 x 0.6 m), placed upstream of the centrifugal fan. The flow rate from 12 to 60 l/s is controled by changing the diameter of a diaphragm orifice. The unsteady aerodynamic pressure was measured at various positions within the impeller-diffuser unit. Kulite type dynamic sensors, with a diameter of 1.6 mm and a band-width of 125 kHz were used. They are placed at the impeller inlet (figure 2: A), the impeller-diffuser interface (figure 2: B), the diffuser centreline (figure 16:) and the return channel outlet (figure 2: C). This allows the measurement of a static pressure up to 140 mbar and a fluctuating component up to 194 dBA. These aerodynamic data are transmitted to a digital oscilloscope (Gould Nicolet: Sigma 90) with 8 simultaneous channels whose band-width is 25 MHz and has a resolution of 12 bits. Figure 3 presents a schematic of the measuring equipment.

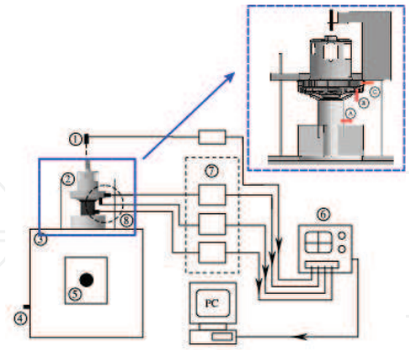

1- Optical tachometer
2- Motor.
3- Box.
4- Static pressure tap.
5- Orifice plate.
6- Digital oscilloscope.
7- Conditioners.
8- Pressure Kulite MIC-062-2D Sensors:
A- Pressure sensor at the impeller inlet.
B- Pressure sensor at the impeller-diffuser interface.
C- Pressure sensor at the return channel outlet.

Fig. 2. Diagram of the test bench

2.3.1 Overall performances and flow field description

Experimental measurements were conducted in order to get the overall and local air-flow characteristics. Two numerical simulations were carried out, the first one does not take into account the cavity between the impeller shroud and the casing, while the second one does. The simulation results relating to the pressure fluctuations in various parts of the fan are compared with the experimental results. For all pressure measurements the uncertainty is ± 2.5 mbar.

Figure 3 represents the evolution of the pressure at the inlet of the impeller and the outlet of the return channel according to the flow rate mesured with an uncertainty of ± 0.4 l/s. At the outlet of the return channel measurements and numerical results are in good agreement. A phenomenon of blocking produce the increase in static pressure with the flow rate. At the impeller inlet, the calculated pressure curve corresponding to a case without cavity between the impeller and the casing, predicts obviously more depression compared to tests and case with cavity, particularly with flow rates from 21 to 40 l/s. The pressure rise difference between cases with and without gap is due to the presence of strong bakflow vortex at the impeller entrance which leads to the reduction in total and static pressure rise (pressure difference between the inlet and the outlet), see Khelladi et al. (2005a). The effect of vortices decreases at partial flows. The pressure curve calculated taking into account the cavity is in good agreement with the experimental results particularly with flow rates greater or in the vincinity of the nominal flow-rate of 35 l/s. When the fan works at partial flow rates the solution is more difficult to achieve accurately, specially because of the presence of separated flows.

At the nominal flow-rate, the difference of static pressure between experimental result, the case without cavity (Case I) and with cavity (Case II) can be respectively assessed to be of 40% and 3% (experimental results are used as reference). Therefore, it can be considered that the numerical model with the cavity is in adequate accuracy with the measurement and that the effect of the cavity on the overall performance can not be ignored.

The modeling of the cavity, specially the meshing procedure is time and resources consuming. Therefore, when the computation aim the determination of global performance of the fan, volumetric losses due to the cavity and more precisely due to the clearance can be separately modeled using the results of the numerical case without cavity.

The first step is to evaluate the pressure p_f prevailing at the ring seals in view to obtain the volumetric losses and the mass flow rate shift due to the backflow through the cavity. The model is based on simple physical considerations traducing radial balance of the force acting on fluid particles in the volume between the rotating shroud and the fix external casing. For simplification, each part is modeled by a disc. Then, let consider the elementary volume of a ring of fluid of internal radius r, external radius(r+dr) and of lateral length b. This volume is submitted to pressure and centrifugal forces respectively $2\pi \cdot r \cdot b \cdot p$ for inward force, $2\pi \cdot b \cdot (p + dp)$ for outward ($2\pi \cdot dr \cdot b(p + dp)$ is neglectible) and $2\pi \cdot r \cdot dr \cdot b \cdot \rho \cdot \omega^2 \cdot r$ for the centrifugal force. Equilibrium involve force balance to be zero in radial direction. The equilibrium equation is given by,

$$2\pi \cdot r \cdot p \cdot b + \rho \cdot 2\pi \cdot r \cdot dr \cdot \omega^2 \cdot r = (p + dp)2\pi \cdot r \cdot b \tag{1}$$

and after simplification,

$$dp = \rho\omega^2 \cdot r \cdot dr \tag{2}$$

The integration of the relation from the exit of the impeller to the clearance located respectively at radius R_2 and R_f provides the expression:

$$p_f = p_2 - \frac{\rho}{8}\omega^2\left(R_2^2 - R_f^2\right) \tag{3}$$

where p_2 is the static pressure that prevails at this location on the theoretical machine. p_f will be used to estimate the head loss due to the leakage: $\Delta p_f = p_f - p_1$. The velocity of the flow between the static and rotating disc vary from zero to ωR_i. The effective velocity of the flow in the clearance is modeled by $k\omega R_i$. The conventional assumption is made that the flow between the static and the rotating surface has almost the characteristics of a Couette flow and $k \approx 0.5$. This proposal has been verified by a simple CFD calculation in an equivalent machine.

The leakage rate qv_f through the gap is calculated by,

$$qv_f = C_f S_j = C_f 2\pi R_f j \tag{4}$$

where C_f is the actual speed of the fluid in the gap.

The velocity C_f is calculated from the expression (5). The first term on the right end side is the loss due to the contraction and expansion through the gap. Factor 1.5 is empirical. The second term on the right is the loss by friction on the length of the ring where j is the hydraulic diameter. L is the axial length of the clearance and λ the friction loss coefficient for a smooth turbulent flow.

$$\frac{\Delta p_f}{\rho} = 1.5\frac{C_f^2}{2} + \lambda\frac{L}{2j}\frac{C_f^2}{2} \tag{5}$$

with,

$$\lambda = \frac{0.316}{\Re e^{1/4}} \text{ and, } \Re e = \frac{C_f 2j}{\nu} \tag{6}$$

The quantity Δp_f is subtracted from the charge of the fan computed without clearance and the flow rate is shifted of qv_f. The final results are confronted figure (3) where it can be seen that the results are in good agreement with experiment on a wider range that the full simulation.

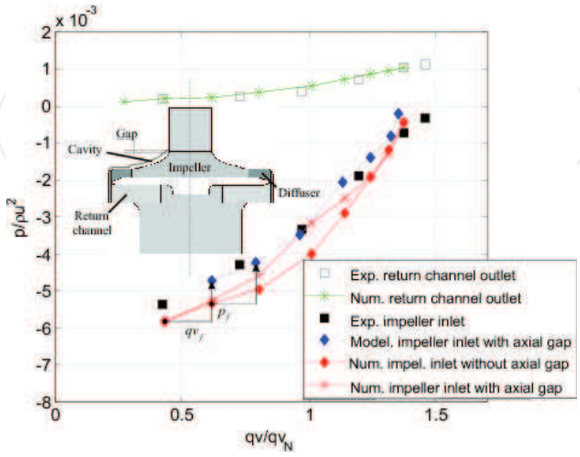

Fig. 3. Comparison of overall performance between calculation and measurement

Figure 4 represents the difference of pressure between experimental measurement, the results of full computation and the results of computation without cavity modified with the model.

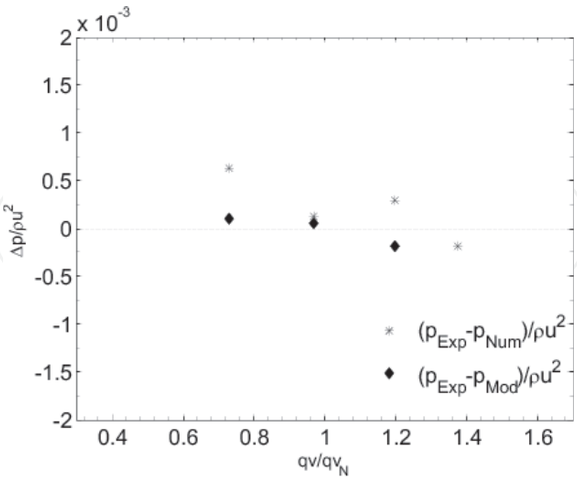

Fig. 4. Pressure difference between measurement and predictions

Figure 5 represents the pressure fluctuation versus time, at point p, as obtained by calculations and tests at the operating point. The uncertainty in time measurement was $\pm 2.5 \times 10^{-6}$s . Notice that the measurement point is located at the midline of two diffuser blades on the impeller-diffuser interface, so that the blade to blade interaction between the impeller and the diffuser and the separation at the blades leading edge of the diffuser do not disturb the measurement.

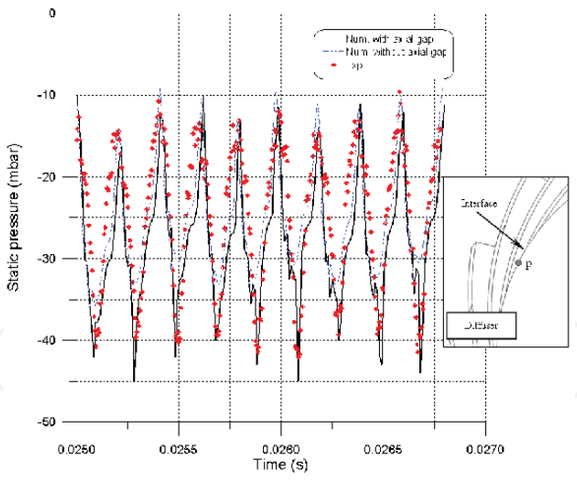

Fig. 5. Variation of the pressure at a point on the impeller-diffuser interface versus time - flow rate = 35 l/s.

On the figure, one distinguishes the impeller blade passage as characterized by pressure peaks. The pressure decreases quickly just after the blade passage and increases gradually with the approach of the following blade. The peak to peak pressure gradient due to the blade impeller passing is very important (30 mbar) compared to (it will be show later) the pressure rise in the entire diffuser. A significant difference between theoretical results with and without cavity is noted at low pressure peaks. The comparison between tests and

numerical simulations validates this result. The calculation result taking into account the cavity is closer to the tests than that without. The general shape of the two calculation results are quite similar, the same curvatures are observed at the same time positions. So the axial cavity only affects the peak to peak pressure gradient.

Figure 16 represents the variation of the static pressure along the centerline of the diffuser as measured by flush mounted sensors that do not disturb the flow. The uncertainty in the curvilinear coordinate distance (s) is ± 0.1 mm.

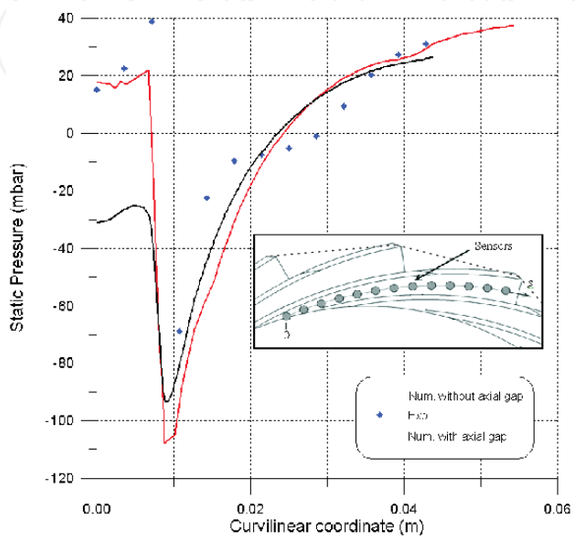

Fig. 6. Evolution of the static pressure in the curvilinear direction along the axial clearance of the diffuser - flow rate = 35 l/s.

The first three points (curvilinear coordinate = 0 to 0.008 m) of measurement in figure 6 are located in a recirculation zone, according to Khelladi et al. (2005a) and the difference between pressure distributions could be seen as a question of static pressure measurment. However, the results of the simulation where the gap is taken into account, is to bee seen mainly in a shift of the pressure rise characteristic. The internal mass flow through the impeller is higher than the mass flow measured at the inlet of the stage due to the leakage flow. This means a given pressure rise across the impeller is attributed to a lower mass flow (internal mass flow trough the impeller minus leakage mass flow). Just after this zone (curvilinear coordinate = 0.008 to 0.01 m) the pressure falls quickly at the leading edge of the diffuser to increase until reaching its maximum value on the outlet side of the diffuser (curvilinear coordinate = 0.01 to 0.045 m). The diffuser transforms a part of the kinetic energy to pressure energy, it increases the pressure from -100 to 30 mbar.

A blade-to-blade section was selected. This sectional view of the static pressure at the section of blade-to-blade at middle radial span (5 mm away from the hub)is shown in figure 7A) and figure 7B) for the Case I and II, respectively. The static pressure difference between the impeller inlet and diffuser outlet can be roughly assessed. The difference for Case I is about twice of the Case II. This implies that the existence of the leakage flow reduces the capability of static pressure rise. The inflow condition to the downstream component(i.e., the diffuser) depends on the flow field at impeller exit. Referring to both cases, it can be found that the flow around one of the diffuser vanes is characterized by the fact that the incidence angle is too positive introducing a strong stagnation point at the suction side near

the leading edge, in turn, it produce an acceleration regime in the opposite side. Naturally, this kind of flow increases both the static loading of the diffuser and the force fluctuation due to impeller/diffuser interaction. Not only the through flow capability but also the overall performance will be degraded due to the flow blockage existing in the diffuser.

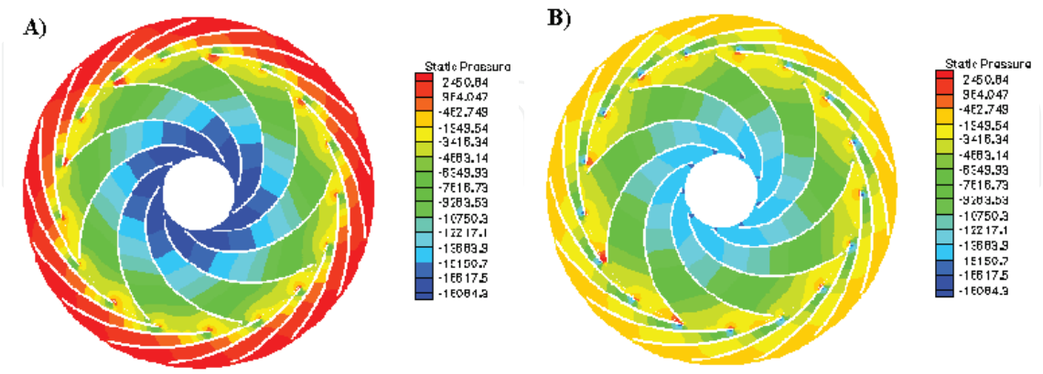

Fig. 7. Comparison of contour of static pressure at a blade-to-blade section of mid radial span for the case, A) without tip clearance and B) with tip clearance

The comparison of the static pressure at the section plotted across the rotating axis for the case with/without cavity is presented in figure 8, figure 8A) and figure 8B) are for Case I and Case II, respectively. The static pressure through the fan inlet and outlet can be roughly figured out for both cases, for Case I it is about 1.3 times bigger than that of Case II. The static pressure is gradually increased from impeller inlet to outlet, inducing a returned flow inside the cavity from the outlet side of impeller back to the inlet and generating a re-circulation flow pattern, see Khelladi et al. (2005a). As can be seen in figure 8B), the static pressure inside the cavity deacrease slowly from the impeller outlet to the gap. At the gap the static pressure of cavity is bigger than that of impeller, which produces an unavoidable source of flow re-circulation distortion ahead of the impeller as well as loss generation.

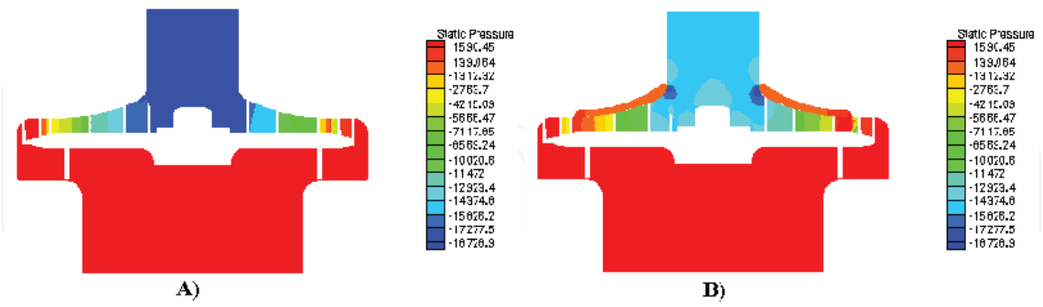

Fig. 8. Comparison of contour of static pressure at a cross-rotating-axis section for the case, A) without tip clearance and B) with tip clearance

The comparison of the total pressure at the cross-rotating-axis section is given in figure 9. The maximum total pressure rise for Case I is roughly 2 times the one of Case II. For Case I, the total pressure is uniformly increased through impeller and diffuser but high distortions are found at the cross-over bend and return channel. For Case II, it exists a non-uniformity at impeller inlet, cross-over bend and return channel. The almost constant total pressure inside the cavity

is found to generate a stagnation point near the impeller inlet. As mentioned-above, the cross-over bend and return channel are two dominant components with high loss generation.

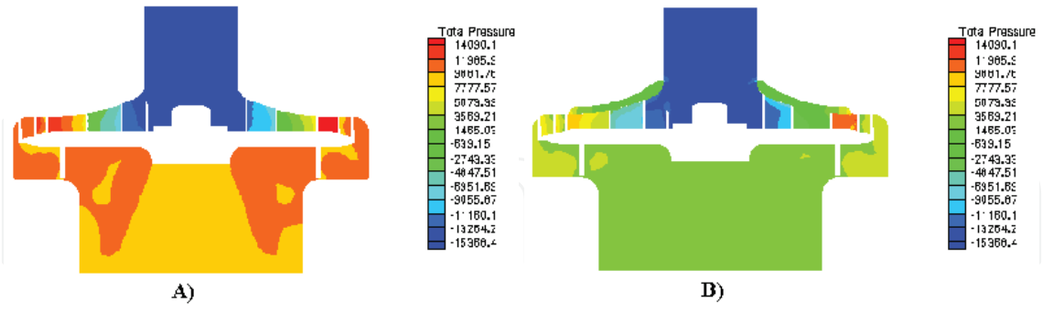

Fig. 9. Comparison of contour of total pressure at a cross-rotating-axis section for the case, A) without tip clearance and B) with tip clearance

Figure 10 shows the solution of entropy for both cases. By this one can be quantitatively understood the loss distribution. For Case I, as shown in figure 10A), very high entropy gradients occur through impeller exit, cross-over bend and return channel. This can also be found in figure 10B) for Case II, typically, a big jump appears at the impeller inlet close to the gap where a strong stagnation point is produced. Due to the high rotating speed, the absolute velocity at impeller exit is so high that a strong swirling flow occurs at the cross-over bend. Due to the narrow frontal area at the cross-over bend and return channel, the strong flow blockage and vortex is accumulated.

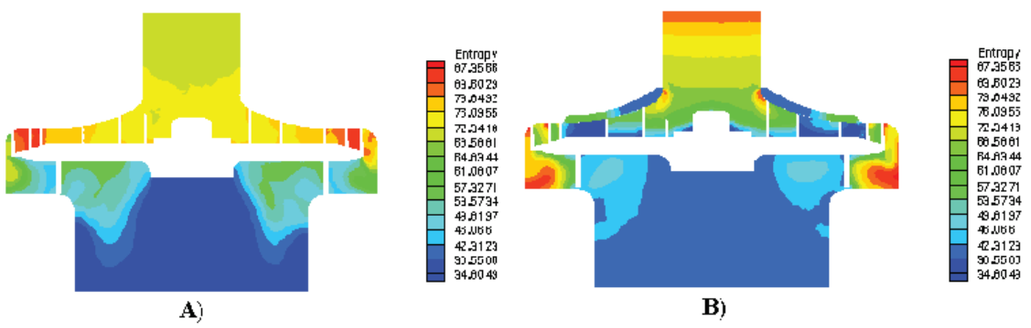

Fig. 10. Comparison of contour of entropy at a cross-rotating-axis section for the case, A) without tip clearance and B) with tip clearance

2.3.2 Loss generation

In order to easily show (quantify) the loss generation for each flow component, a half view of the flow components into the centrifugal fan is schematically plotted as shown in figure 11. The impeller inlet is indicated by *A* in the figure and the diffuser by *B*. The cross-over bend is indicated by *C*. *D* region is the return channel and the downstream duct is indicated by *E*.

The vorticity amplitude for each component is normalized by that of the impeller outlet. As shown in figure 12 (Case I), the maximum vorticity amplitude occurs at the impeller due to its high rotating speed. *A*, *B* and *C* regions have equivalent ones with about half of the one of the impeller implying a strong swirling flow and is probably the cause of flow blockages and total pressure drop.

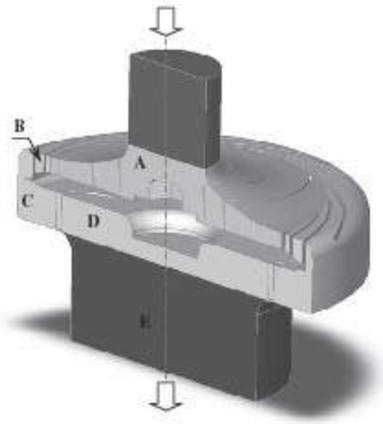

Fig. 11. Schematic of the calculation domain with the flow components of the centrifugal fan (half view)

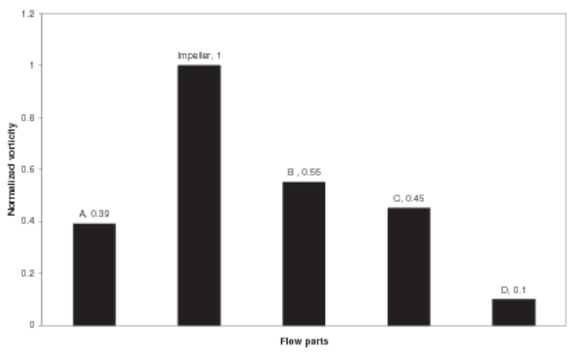

Fig. 12. Distribution of normalized vorticity amplitude along the centrifugal fan (Case I)

The static pressure rise coefficient for the stationary compartment can be written as

$$C_p = \frac{P_{s2} - P_{s1}}{P_{t1} - P_{s1}} \tag{7}$$

Where subscripts 's' denotes static pressure, 't' the total pressure, '2' the exit section of the component, and '1' the inlet section of the component. The static pressure recovery coefficient along the stationary parts of Case I is shown in figure 13. In this case, the maximum pressure recovery, around 0.53, occurs at the cross-over bend. Both A and D regions have the same pressure recovery, around 0.15.

The loss coefficient for the stationary parts is given by

$$\omega = \frac{P_{t2} - P_{t1}}{P_{t1} - P_{s1}} \tag{8}$$

In figure (14) one can see that the main part of losses occurs in the return channel and the cross over bend. This is due to the flow separation resulting from the strong meridional curvature and by the 90 degree change of direction of the flow. The comparison between cases I and II is listed in Table 3. We can observe that for Case I the maximum loss occurs at the cross-over

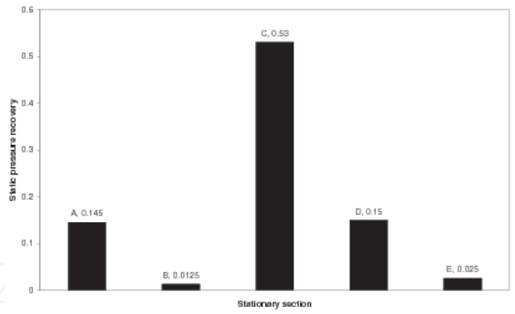

Fig. 13. Static pressure recovery for stationary sections (Case I)

bend while it moves downstream to the return channel for Case II. This is due to the severe flow blockage occurring in Case II.

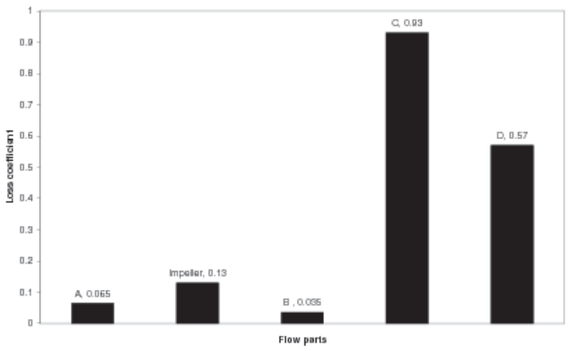

Fig. 14. Distribution of total pressure loss along the centrifugal fan (Case I)

Section	Case I	Case II
A	0.065	0.50
Impeller	0.13	0.14
B	0.035	0.79
C	0.93	0.79
D	0.57	0.97

Table 3. Comparison of loss distribution into the centrifugal fan components

The isentropic efficiency of the impeller is defined as

$$\eta = \frac{\left(\frac{P_{t2}}{P_{t1}}\right)^{\frac{\gamma-1}{\gamma}} - 1}{\frac{T_{t2}}{T_{t1}} - 1} \tag{9}$$

Considering the viscous effect to the total pressure rise, the total pressure coefficient can be expressed as

$$\pi = \tau^{\frac{\gamma-1}{\gamma}} \exp\left(\frac{-\Delta s}{R}\right) \tag{10}$$

where $\tau = 1 + \frac{U_2 C_{\theta 2}}{C_p T_{t1}}$, U_2 is the rotating velocity at the impeller exit, $C_{\theta 2}$ is the circumferential component of the absolute velocity at the impeller exit, T_{t1} is the total temperature at the impeller inlet. Δs is the entropy increment and R is the gas constant. The calculated overall

performances for both cases are listed in Table 4. It is found that the total efficiency has 1% drop when the cavity is taken into account, meanwhile, both the total-pressure ratio and temperature ratio drop too.

	Case I	**Case II**
η (total-total efficiency)	0.87	0.86
π (total-total pressure ratio)	1.15	1.12
τ (total temperature ratio)	1.065	1.057

Table 4. Comparison of overall performance between Case I and Case II

2.4 Concluding remarks

In this section, a rotational speed centrifugal fan with compact dimensions was studied numerically and experimentally. The computational models with/without cavity (between the shrouded impeller and the fixed outer casing) were set up for unsteady solutions. A volumetric loss model was coupled to the case without cavity and compared to the later configurations. The effects of the cavity on the calculated flow field and the loss generation were qualitatively analyzed. The comparison of fan performances between the prediction and measurement showed a favorable tendency. The result obtained by the volumetric loss model, which is easy to setup, coupled to the configuration without cavity gives as good result as the computational model with cavity. This result can be very interesting knowing that the model with cavity is more consumptive in grid size and computational effort than the case without cavity. In terms of the flow restriction obtained for the centrifugal fan, a new empirical constant accounting for the effects of a cavity on the flow restriction of the centrifugal fan system was approximated. In presence of the cavity, due to the difference of static pressure, a leakage flow due the clearance appears and is injected in the main stream at the impeller inlet. Subsequently, a stagnation point appears and changes the incidence angle and then the flow performances as well.

3. Aeroacoustic study

3.1 Computational aeroacoustics for compelex geometries – application to subsonic turbomachines

The sound generation by a flow and its propagation are a matter of aerodynamics. Indeed, the conservation equations of mass and momentum govern both the flow dynamics and the resulting acoustic phenomena. However, the features of the aerodynamic flow and the sound are different. The first is convective and/or diffusive and the second is propagative with very low attenuation due to viscosity. On the other hand, aeroacoustic problems present a wider range of wave-lengths than those of aerodynamic ones.

Aeroacoustic noise optimization is the main topic of many widespread research studies of industrial interest, see Khelladi et al. (2008); Maaloum et al. (2004) works. In fact, the noise level emitted by a device could determine the success or failure of a new prototype. On the other hand turbomachines are widely found in industrial applications. In these devices the level of sound generated is a very important parameter of design.

The prediction of aerodynamic noise benefits from recent developments in numerical methods and computer science. However, despite the knowledge accumulated over the past few

decades on the mechanisms of noise generation on complex systems as for example air delivery systems, the prediction of such a flow field and the resulting acoustic pressure, by numerical methods is still difficult. This is due to our inability to model the turbulent viscous flow with enough accuracy on complex geometries and to the complicated nature of flow through turbomachines. Until now, there is still no consensus about the aeroacoustic approach to adopt, and actually, it depends on the application. In the following we present a succinct description of the most commonly used approaches.

Previously to our exposition, we recall the concepts of far and near-fields. The concept of far-field, relative to the effects of the flow compressibility, concerns the propagation of acoustic waves produced by a pressure change in the propagation medium. The occurred disturbance propagates gradually by molecular excitement to the observer far from the source. Unlike the far-field, near-field includes the sound due to the fluid compressibility and another component called the aerodynamic disturbance field or pseudo-sound. It consists of all pressure fluctuations governed primarily by the incompressibility directly related to the flow. These fluctuations are local and are not propagative.

In Computational Aeroacoustics (CAA), two computational approaches are possible:

Direct approach

This approach consists of adjusting the aerodynamic numerical modeling to the acoustics requirements. In other words, it is needed to use numerical schemes adapted to the acoustic propagation, providing low-dissipation and low-dispersion. However, the complexity of implementing these schemes and the far field constraint, where the grid must extend over very large distances, greatly increases the computational costs and makes using this approach very difficult for complex geometries.

Hybrid approach

This approach can be divided into two types of modelling.

- The first one is to use the direct approach near disturbances in which the acoustic waves are propagated over a short distance. They are then propagated using an adapted propagation operator, as Kirchhoff's equation, according to Farassat & Myers (1988), for example, to the far field. For adapted wave operator we mean a wave equation or other conservation equation system that permits an acoustic wave to propagate from a given acoustic source. However, the simulation of the flow field requires DNS or LES, and the treatment of boundary conditions must be done with utmost care to ensure an accurate transition between near and far fields.
- The second consists of separating aerodynamics and acoustics computations. Thus, acoustic sources are given by aerodynamic calculation and propagated using wave equation (Ffowcs Williams & Hawkings (1969), Kirchhoff,...), linearized Euler equations or other approaches like LPCE presented by Moon & Seo (2006),.... The constraints and the computation time is considerably reduced compared to DNS.

Aeroacoustics of complex geometries

Aeroacoustics is a science dealing with the sound generated either by the flow itself, as free jet turbulence or by its interaction with a moving or static surface, rigid or deformable,

as fan blades, helicopter rotor, compressors or turbines, etc. Thus, in these latter kinds of applications, we need to deal with flow through complex geometries.

The first attempt to formulate a theory about the acoustics of propellers was conducted by Lynam & Webb. (1919). They showed that the rotation of the blades of a propeller causes a periodic modulation of the fluid flow and associated acoustic disturbance. Another approach, initiated by Bryan (1920), is to study the propagation of a source point in uniform motion. This had as main feature the introduction of the concept of delayed time.

Gutin (1948) was the first to establish a theoretical formalism of a steady noise source through linear acoustics. He showed that steady aerodynamic forces correspond to dipole source distribution on the disc of a propeller. This model proves to be incomplete because, in reality, the noise emitted by rotating blades extends rather high frequencies. The sound at high frequencies is a consequence of the unsteadiness of aerodynamic loads.

Advances in the prediction of noise from the airflow, are based on of Lighthill (1952; 1954) investigations. In his analogy, the generated noise is mathematically reduced to the study of wave propagation in a medium at rest, in which the effect of the flow is replaced by a distribution of sources. The pressure is therefore regarded as characterizing a sound field of small amplitude carried by a fluid, whose properties are uniform throughout the area at rest. The major intake of Lighthill is to include nonlinear terms expressing the noise generation by turbulent flow.

Curle (1955) extended the Lighthill's analogy to include solid boundaries by treating them as distributions of surface loads. Subsequently, Ffowcs Williams & Hawkings (1969) (FW&H) have extended this approach by taking into account the motion of solid surfaces in the flow.

Far and near-fields

The concept of far-field, relative to the effects of the flow compressibility, concerns the propagation of acoustic waves produced by a pressure change in the propagation medium. The occurred disturbance propagates gradually by molecular excitement to the observer located far from the source.

Unlike the far-field, near-field includes the sound due to the fluid compressibility and another component called the aerodynamic disturbance field or pseudo-sound. It consists of all pressure fluctuations governed primarily by the incompressibility directly related to the flow. These fluctuations are local and are not propagative.

3.2 Limits of aeroacoustic analogy and alternative approaches

In the common formulation of aeroacoustic analogy solution, the noise is radiated in free and far field. As strong hypotheses: reflections, diffractions, scattering as well as the confinement effects are not taken into account. These hypotheses make very easy the use aeroacoustic analogy for noise prediction of open rotors or free jets for example, but they are also its weaknesses in case of confining. In paper of Khelladi et al. (2008) it was shown that using the FW&H formulation to model the noise generated by a centrifugal fan does not match measurements because of the presence of a casing. Taking into account the sound attenuation of the casing to correct the directivity has not really solved the problem. For this kind of problems, it was therefore concluded that the aeroacoustic analogy does not obtain accurate results.

To take into account confining effects, it is expected that LEE can give satisfactory results. In fact, with LEE one can use the same acoustic sources as FW&H for example, and in addition reflections, diffractions and scattering are naturally taken into account by an adequate choice of boundary conditions.

In fact, figure (15) shows the predicted overall sound level compared to measurements of the centrigugal fan presented above into the aerodynamic section. The difference between the overall sound level and mesurements is presented in figure (16). As shown in this figure, the difference between measurements and calculation is about 10 dB (over a maximum value of 110 dB) at the radial direction around 90° and 270°, the calculation predict more noise at this direction than measurements. In addition to the assumptions stated above, the reason is that in the theoretical model all the surfaces are considered as acoustically transparent, the effect of the acoustic attenuation of the diffuser blades in the radial direction is not taken into account. In the axial direction, the difference do not exceed 5 dB by taking into account the attenuation of the casing. In this direction the fan radiates in free field.

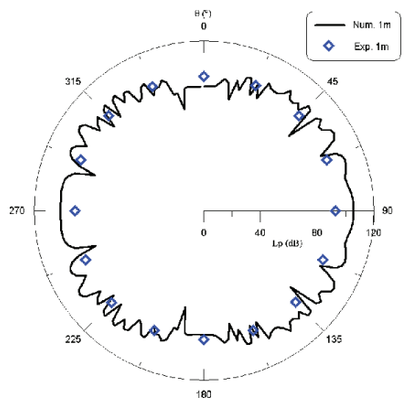

Fig. 15. Numerical and experimental overall noise directivity - $m = 1$, $r_0 = 1$ m, $\varphi = \pi/4$.

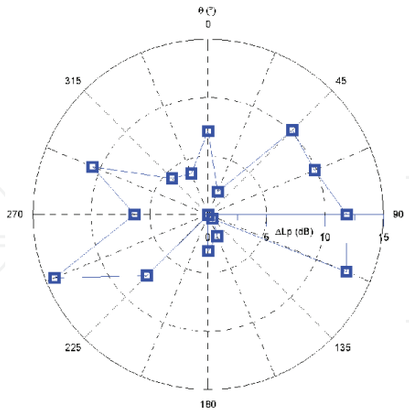

Fig. 16. Difference between directivities obtained by the measurements and the calculations ($\Delta L_p = \left| L_{p_{exp}} - L_{p_{num}} \right|$) at $m = 1$, $r_0 = 1$ m and $\varphi = \pi/4$.

To take into account confining effects, it is expected that LEE can give satisfactory results. In fact, with LEE not only one can uses the same acoustic sources as FW&H for example, but also reflexions, diffractions and scattering are naturally taken into account by an adequate choice of boundary conditions.

3.3 Linearised Euler equations

In many aeroacoustic applications we can assume that problems are linear, see Colonius & Lele (2004). In those cases, it is possible to linearize the Euler equations around a (mean) stationary solution $\boldsymbol{U}_0 = (\rho_0, u_0, v_0, p_0)$. Thus, we can write the Linearized Euler Equations written in conservative form are the following:

$$\frac{\partial \boldsymbol{U}}{\partial t} + \frac{\partial \boldsymbol{F}}{\partial x} + \frac{\partial \boldsymbol{G}}{\partial y} + \boldsymbol{H} = \boldsymbol{S} \tag{11}$$

being $\boldsymbol{S}$ a source term and

$$\boldsymbol{U} = \begin{pmatrix} \rho \\ \rho u \\ \rho v \\ p \end{pmatrix} \qquad \boldsymbol{F} = \begin{pmatrix} \rho u_0 + \rho_0 u \\ p + \rho_0 u_0 u \\ \rho_0 u_0 v \\ u_0 p + \gamma p_0 u \end{pmatrix} \qquad \boldsymbol{G} = \begin{pmatrix} \rho v_0 + \rho_0 u \\ \rho_0 v_0 u \\ p + \rho_0 v_0 v \\ v_0 p + \gamma p_0 v \end{pmatrix} \tag{12}$$

$$\boldsymbol{H} = \begin{pmatrix} 0 \\ (\rho_0 u + u_0 \rho) \dfrac{\partial u_0}{\partial x} + (\rho_0 v + v_0 \rho) \dfrac{\partial u_0}{\partial y} \\ (\rho_0 u + u_0 \rho) \dfrac{\partial v_0}{\partial x} + (\rho_0 v + v_0 \rho) \dfrac{\partial v_0}{\partial y} \\ (\gamma - 1)\, p \boldsymbol{\nabla} \cdot \boldsymbol{\nu}_0 - (\gamma - 1)\, \boldsymbol{\nu} \cdot \boldsymbol{\nabla} p_0 \end{pmatrix} \tag{13}$$

where $\boldsymbol{\nu} = (u, v)$, $\boldsymbol{\nu}_0 = (u_0, v_0)$, ρ is the density, p the pressure and $\gamma = 1.4$. Subscript $_0$ is referring to mean values. In case of an uniform mean flow, $\boldsymbol{H}$ is null. To solve these equations, we need to compute previously the acoustic sources S, by using LES or DNS. Bogey et al. (2002) presented a methodology to compute the sources.

To solve the above system which is a hyperbolic system, we used FV-MLS method presented and commented by Khelladi et al. (2011). The FV-MLS is a new high order finite volume method for unstructured grids based on moving least squares approximation, it was demonstrated that this method is particularly efficient for this kind of hyperbolic systems. Concerning the numerical developments, we choose to present only the construction of boundary conditions which are one of the most critical points of this kind of problems.

3.4 Boundary conditions

In CAA the treatment of boundary conditions plays a key role according to Colonius et al. (1993), since even small spurious disturbances when the waves leave the domain can distort the acoustic field. In the following we expose our approach to the boundary conditions. For our modeling, the boundary conditions enter in the discretized equations through a proper definition of the numerical flux that can be written as $\boldsymbol{H}(\boldsymbol{U}^+, \boldsymbol{U}^{*-}, \boldsymbol{n})$, where $\boldsymbol{n}$ points outward from the domain and $\boldsymbol{U}^{*-}$ is the external state variable. Depending on the boundary type, the construction of $\boldsymbol{U}^{*-}$ accounts for, both, the physical boundary conditions that must be enforced and the information leaving the domain.

3.4.1 Reflecting boundary conditions

A perfectly reflecting boundary condition is easily obtained by defining, at each Gauss points on the rigid wall boundaries, an external mirror fictitious state $\boldsymbol{U}^{*-}$.

The external state is then expressed as

$$\boldsymbol{U}^{*-} = \boldsymbol{R}\boldsymbol{U}^{+} \tag{14}$$

where $\boldsymbol{R}$ is a transition matrix function of $\boldsymbol{n}$'s components, it reads

$$\boldsymbol{R} = \begin{pmatrix} 1 & 0 & 0 & 0 \\ 0 & 1-2n_x^2 & -2n_x n_y & 0 \\ 0 & -2n_x n_y & 1-2n_y^2 & 0 \\ 0 & 0 & 0 & 1 \end{pmatrix} \tag{15}$$

Using this condition, the mass flux computed by the Riemann solver is zero and the non-permeability condition is satisfied.

3.4.2 Absorbing boundary conditions

Constructing absorbing (non-reflecting) boundary conditions for CAA is pretty delicate because of the high sensitivity of the accuracy to the small spurious wave reflexions at far field boundaries. Approaches based on the characteristics theory are not suited for CAA problems, other approaches, such as Perfectly Matched Layers (PML), presented by Hu (1996), and radial boundary condition of Tam & Webb (1993) are more indicated and widely discussed in the literature for finite differences schemes.

In this work we employ upwinding technique used by Bernacki et al. (2006) with DG to select only outgoing waves at the outer boundaries. Intuitively, it means that whole waves energy is dissipated at boundaries but unfortunately nothing prove that energy is actually dissipated and no spurious wave reflexions persist. To overcome this inconvenient, we join to the above procedure a grid stretching zone, see Nogueira et al. (2010). Grid stretching transfers the energy of the wave into increasingly higher wavenumber modes and the numerical scheme removes this high-frequency content. With this process most of the energy of the wave is dissipated before reaching the boundaries. For a high wavenumber the numerical method introduces more dissipation.

At the grid stretching zone, it is possible to use the MLS method as a filter in unstructured grids. The filtering process is developed by the application of a MLS reconstruction of the variables, i.e:

$$\bar{\boldsymbol{U}}(\boldsymbol{x}) = \sum_{j=1}^{n_{x_I}} \boldsymbol{U}(\boldsymbol{x}) N_j(\boldsymbol{x}) \tag{16}$$

where, $\boldsymbol{U}$ is the reconstructed variable, $\bar{\boldsymbol{U}}$ is the filtered variable and N is the MLS shape function. This reconstruction is performed by using a kernel with shape parameters favoring dissipative behavior that the ones used to the approximation of the variables. The value of these parameters determines the range of frequencies to be filtered.

At the outer boundaries, we propose the following explicit numerical flux,

$$\boldsymbol{H}(\boldsymbol{U}^n, \boldsymbol{U}^{*n}, \boldsymbol{n}) = \frac{1}{2}(\mathbb{F}(\boldsymbol{U}^n) \cdot \boldsymbol{n} + |\mathbb{P}|\boldsymbol{U}^{n-1}) \tag{17}$$

with,
$\boldsymbol{U}^{*n}$ is the fictitious state corresponding to the absorbing side ensuring $\mathbb{P}\boldsymbol{U}^{*n} = |\mathbb{P}|\boldsymbol{U}^{n-1}$, $\mathbb{P}$ is

the Jacobien matrix of system (11) and $|\mathbb{P}| = \mathbb{V}^{-1}|\mathbb{D}|\mathbb{V}$, $\mathbb{D}$ and $\mathbb{V}$ are respectively, eigenvalues diagonal matrix and eigenvectors matrix of $\mathbb{P}$. $|\mathbb{P}|$ is then given by,

$$|\mathbb{P}| = \begin{pmatrix} L_3 & \frac{n_x}{2c_0}(-L_1+L_2) & \frac{n_y}{2c_0}(-L_1+L_2) & \frac{-1}{c_0^2}L_3 + \frac{1}{2c_0}(L_1+L_2) \\ 0 & \frac{n_x^2}{2}(L_1+L_2)+n_y^2 L_4 & \frac{n_x n_y}{2}(L_1+L_2-2L_4) & \frac{n_x}{2c_0}(-L_1+L_2) \\ 0 & \frac{n_x n_y}{2}(L_1+L_2-2L_4) & \frac{n_y^2}{2}(L_1+L_2)+n_x^2 L_4 & \frac{n_y}{2c_0}(-L_1+L_2) \\ 0 & \frac{n_x c_0}{2}(-L_1+L_2) & \frac{n_y c_0}{2}(-L_1+L_2) & \frac{1}{2}(L_1+L_2) \end{pmatrix} \tag{18}$$

where,

$$\begin{aligned} L_1 &= |\boldsymbol{V_0}\cdot\boldsymbol{n} - c_0| \\ L_2 &= |\boldsymbol{V_0}\cdot\boldsymbol{n} + c_0| \\ L_3 = L_4 &= |\boldsymbol{V_0}\cdot\boldsymbol{n}| \end{aligned} \tag{19}$$

with, $\boldsymbol{V}_0 = (u_0, v_0)$ and c_0 the speed of sound.

3.5 Application

3.5.1 Validation - convected monopole

This case reproduces the example of Bailly & Juvé (2000). The radiation of a monopole source is computed in a subsonic mean flow, with Mach number $M_x = 0.5$. The source is located at $x_s = y_s = 0$, and is defined as:

$$S_p = \frac{1}{2}\exp\left(-ln(2)\frac{(x-x_s)^2+(y-y_s)^2}{2}\right)\sin(\omega t)\times[1,0,0,1]^T \tag{20}$$

where the angular frequency is $\omega = 2\pi/30$ and t is the time coordinate. The wave length is $\lambda = 30$ units, and the computational domain is a square with 200 units for each side. The source term is made dimensionless with $\left[\rho_0 c_0/\Delta x, 0, 0, \rho_0 c_0^3/\Delta x\right]^T$. With the aim of testing the stability and the behavior of the proposed method for the boundary conditions, an unstructured grid absorbing layer has been added. The absorbing layer is placed from the boundary of the computational domain to $x = \pm 300$ and $y = \pm 300$. In figure 17 (top) it is shown the grid used for the resolution of this problem. To build this grid, 800 equally spaced nodes at the circumference of the computational domain are used and 120 nodes at the outer boundaries circumference.

In addition to the absorbing boundary condition given by equation (17), the shape filter parameters of the absorbing layer are $\kappa_x = \kappa_y = 8$, see Nogueira et al. (2010) paper.

A 5th order mass matrix based FV-MLS solver is used for this example.

Two acoustic waves propagate upstream and downstream of the source, and due to the effect of the mean flow, the apparent wavelength is modified and it is different upstream ($\lambda_1 = (1-M_x)\lambda$) and downstream ($\lambda_2 = (1+M_x)\lambda$) of the source.

In figure 18 pressure isocontours for different non-dimensional times t are shown. The pressure profile along axis $y = 0$ at time $t = 270$ is reproduced in figure 19, and also match the results in Bailly & Juvé (2000).

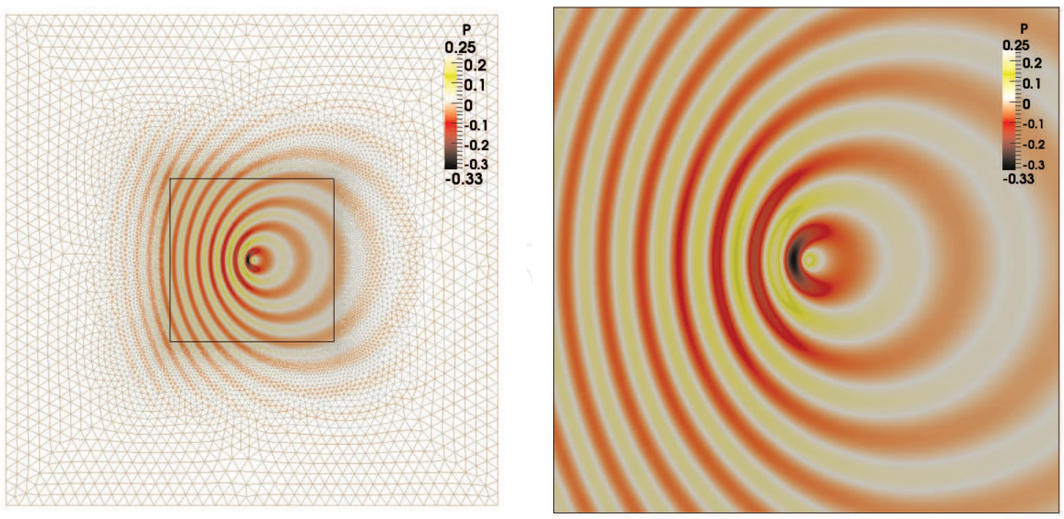

Fig. 17. Convected monopole - M=0.5, 200 × 200 grid, $t = 270$ at $y = 0$

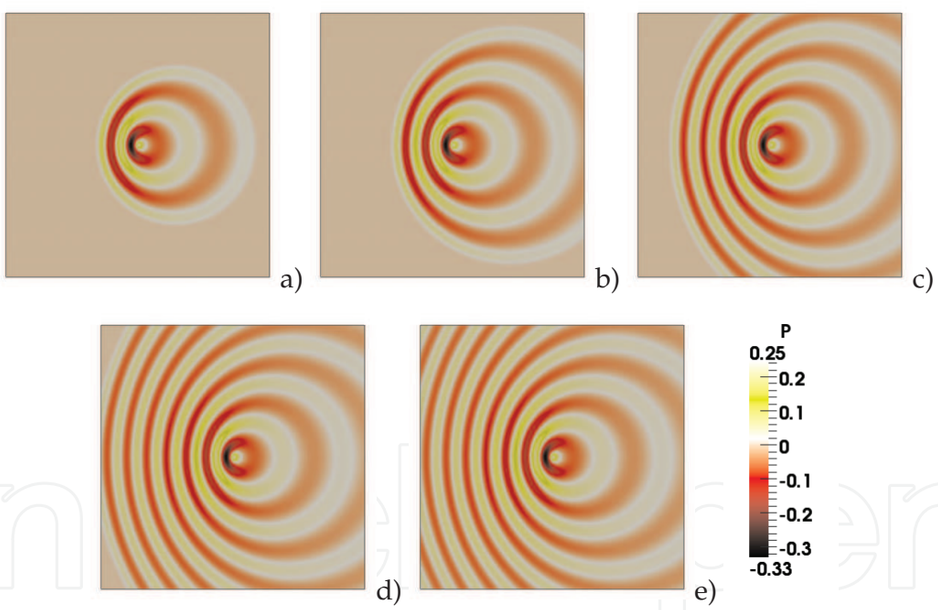

Fig. 18. Convected monopole - M=0.5, 200 × 200 grid. a) t=60, b) t=90, c) t=150, d) t=210, e) t=270

In order to check the stability of the boundary conditions, we let the computations to continue until 180 periods of the source. This time corresponds to the travel of the wave until the four outer boundaries. Comparing the pressure field with the one corresponding to $t = 270$ (9 source periods), it is observed that there is no change in the solution. The acoustic wave is completely dissipated by teh buffer zone when it lefts the computational domain, see figure (17) (top).

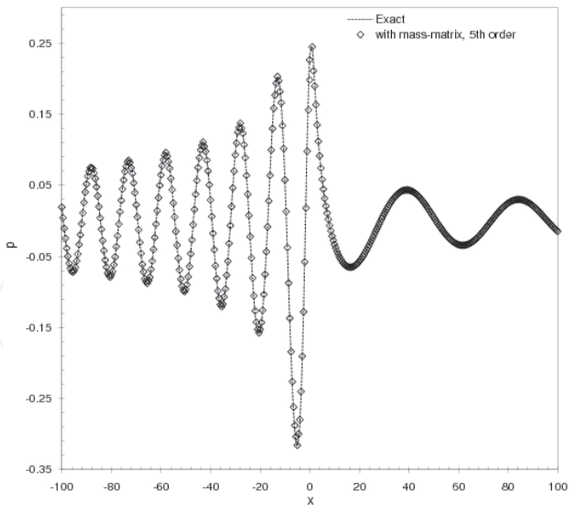

Fig. 19. Convected monopole - M=0.5, 200 × 200

3.5.2 Acoustic waves propagation into a centrifugal fan

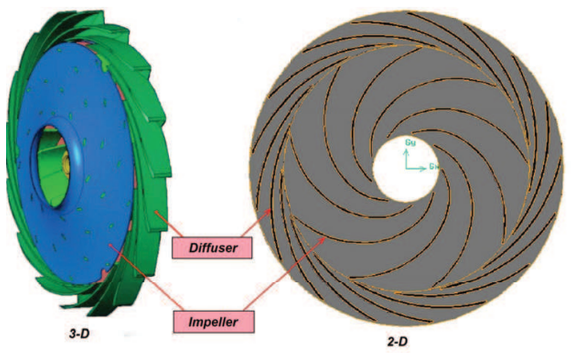

Fig. 20. 3D and 2D centrifugal fan geometric

The centrifugal fan noise is usually dominated by tones produced by the impeller blade passage. The resulted tonal noise corresponds to the blade passage frequency (BPF) and its higher harmonics. This is a consequence of the strong interaction between the impeller and the diffuser blades at their interface.

Shrouded impellers are usually used in high-rotational speed centrifugal fans. The impellers are linked downstream by a vaned diffuser , see figure (20).

A methodology based on a hybrid modeling of the aeroacoustic behavior of a high-rotational speed centrifugal fan is presented in this section. The main objective is to visualize the wave propagation into this machine and demonstrate, then, the power of the proposed methodology. Linearized Euler's equations are used to propagate noise radiated by the rotor/stator interaction. The fluctuating forces at the interaction zone are obtained by an aerodynamic study of the centrifugal fan presented by Khelladi et al. (2005a; 2008). In this section we calculate the acoustic wave propagation of a centrifugal fan with a 9-bladed rotor and a diffuser with 17 blades, as shown in Fig. 13. For the computations we use an unstructured grid, with at least 10 points per wavelength. A detail of the unstructured grid used in this problem is shown in figure (21).

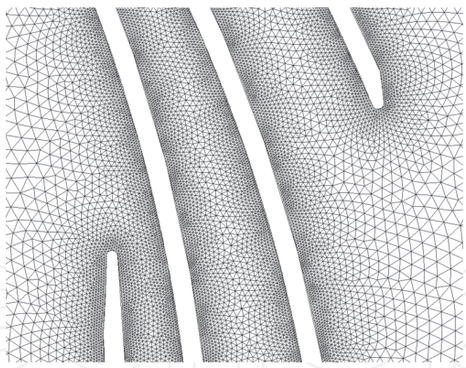

Fig. 21. 2D centrifugal fan mesh

Sources modeling

If we refer to FW&H analogy, one can identify three acoustic sources of three different natures:

- Monopole or thickness source: it is a surface distribution due to the volume displacement of fluid during the motion of surfaces.
- Dipole source or loading source: it is a surface distribution due to the interaction of the flow with the moving bodies
- Quadrupole source: it is a volume distribution due to the flow outside the surfaces.

When the quadrupole source is included, substantially more computational resources are needed for volume integration. However, in many subsonic applications the contribution of the quadrupole source is small. Thus, we have neglected it in this calculation. Moreover, the monopolar source is also neglected at low Mach numbers and small surface thickness.

In our case, the interaction between the impeller and the diffuser blades is the main source of noise radiated by the centrifugal fan, see Khelladi et al. (2008). It is expressed by a pres- sure fluctuation on impeller and diffuser blades. It is, then, of a dipolar nature. This study takes into account only sources located at trailing edge of impeller blades and at the leading edge of blades of diffuser. The rotation of the impeller blades is modeled by rotating sources. Impeller blades are not taken into account in the propagation zone. Thus, we place 17 stationary bipolar acoustic sources located at the leading edge of the blades of diffuser and 9 additional rotating impeller sources located at the trailing edge of each impeller blade.

As for FW&H analogy, the source terms introduced in the LEE are constructed from the momentum equations, and defined by:

$$S_{p_i}(x,y,t) = e^{-\frac{ln(2)}{2}\left[\left(x-x_{s_i}(x,y,t)\right)^2+\left(y-y_{s_i}(x,y,t)\right)^2\right]} \times p_i(t) \times \left[0, n_{x_i}, n_{y_i}, 0\right]^T \tag{21}$$

the subscribe i corresponds to blades id, the position of the of the sources are defined by there coordinates $(x_s(x,y,t), y_s(x,y,t))$. For the impeller the sources moves following a circle path, the diffuser sources are static. $p_i(t)$ is the aerodynamic static pressure and (n_x, n_y) are the components of the unit radial vector at sources (x_s, y_s). The exponential term of equation 21 models the punctual nature of the considered sources.

Acoustic pressure history is presented in figure 22. At the beginning of the simulation we can observe clearly the position of sources. But soon we lose track of them because of reflections

and interference. Thus, all these effects will be explicitly represented in the far field. Note that they are not represented when other approach is used (FW&H, for example).

Fig. 22. Acoustic pressure history

3.6 Conclusion

In this section, we presented the aeroacoustic analysis of the centrifugal fan studied aerodynamically above. For this kind of machines, the effect of the near-field (casing and confinement) is very important which makes it very difficult to use acoustic analogy techniques. Linearized Euler equations seem to be a good alternative. In this section we presented the first developments and results concerning this approach with complex geometries such as the fan we analyzed. Nevertheless, the effect of rotating blades of the impeller was modeled by rotating sources, only the stator is taken into account. Taking into account the moving parts into the propagation domain is a our challenge for the near future. A technique based on sliding mesh method is under-development, the first results were very promising but some difficulties subsist to maintain the overall space order of accuracy due to the rotor/stator interface stencil reconstructions.

4. References

Bailly, C. & Juvé, D. (2000). Numerical solution of acoustic propagation problems using linearized Euler equations, *AIAA Journal* 38(1): 22–29.

Bardina, J., Huang, P. & Coakley, T. (1997). Turbulence modeling, validation, testing and development, *NASA Technical Memorandum 110446* .

Bernacki, M., Lanteri, S. & Piperno, S. (2006). Time-domain parallel simulation of heterogeneous wave propagation on unstructured grids using explicit, non-diffusive, discontinuous Galerkin methods, *J. Computational Acoustics* 14(1): 57–82.

Bogey, C., Bailly, C. & JuvÃl', D. (2002). Computation of flow noise using source terms in linearized eulerÂŠs equations., *AIAA Journal* 40(2): 235–243.

Bryan, G. H. (1920). The acoustics of moving sources with application to airscrews., *R. & M. No. 684, British A.R.C.* .

Colonius, T. & Lele, S. (2004). Computational aeroacoustics: progress on nonlinear problems of sound generation., *Prog Aerosp Sci* 40: 345–416.

Colonius, T., Lele, S. & Moin, P. (1993). Boundary conditions for direct computation of aerodynamic sound generation, *AIAA Journal* 31(9): 1574–1582.

Curle, N. (1955). The influence of solid boundaries upon aerodynamic sound, *Proceedings of the Royal Society of London* A231: 505–514.

Eum, H.-J. & Kang, S.-H. (2002). Numerical study on tip clearance effect on performance of a centrifugal compressor, *Proceedings of ASME FEDSM'02, Montreal, Quebec, Canada, July 14-18* .

Farassat, F. & Myers, M. K. (1988). Extension of kirchhoff's formula to radiation from moving surfaces, *J. Sound and Vib.* 123: 451–560.

Ffowcs Williams, J. & Hawkings, D. (1969). Sound generation by turbulence and surfaces in arbitrary motion, *Philosophical Transactions for the Royal Society of London* A264: 321–342.

FLUENT (1998). Fluent, inc.

Gutin, L. (1948). On the sound field of a rotating propeller, *NACA TM1195, (Traduction de "Über das Schallfeld einer rotierenden Luftschraube", Physikalische Zeitschrift der Sowjetunion, Band 9, Heft 1, 1936).* pp. 57–71.

Hu, F. (1996). On absorbing boundary conditions for linearized Euler equations by a perfectly matched layer, *Journal of Computational Physics* 129: 201–219.

Ishida, M. & Surana, T. (2005). Suppression of unstable flow at small flow rates in a centrifugal fan by controlling tip leakage flow and reverse flow, *Transaction of the ASME Journal of Turbomachinery, Vol. 127, Jan., 76-83* .

Khelladi, S., Kouidri, S., Bakir, F. & Rey, R. (2005a). Flow study in the impeller-diffuser interface of a vaned centrifugal fan, *Journal of Fluid Engineering* 127: 495–502.

Khelladi, S., Kouidri, S., Bakir, F. & Rey, R. (2005b). A numerical study on the aeroacoustics of a vaned centrifugal fan, *ASME Heat Transfer/Fluids Engineering Summer Conference, Houston, Texas* FEDSM2005-77134.

Khelladi, S., Kouidri, S., Bakir, F. & Rey, R. (2008). Predicting tonal noise from a high rotational speed centrifugal fan, *Journal of Sound and Vibration* 313, Issues 1-2: 113–133.

Khelladi, S., Nogueira, X., Bakir, F. & Colominas, I. (2011). Toward a higher order unsteady finite volume solver based on reproducing kernel methods, *Computer Methods in Applied Mechanics and Engineering* 200(29-32): 2348 – 2362.
URL: *http://www.sciencedirect.com/science/article/pii/S0045782511001344*

Kim, K. & Seo, S. (2004). Shape optimisation of forward-curved-blade centrifugal fan with navier-stokes analysis, *Journal of Fluid Engineering* 126: 735–742.

Krain, H. (2005). Review of centrifugal compressor's application and developement, *Journal of Turbomachinery* 127: 25–34.

Lazzaretto, A. (2003). A criterion to define cross-flow fan design parameters, *Journal of Fluids Engineering, Vol.125, 680-683* .

Lazzaretto, A., Toffolo, A. & Martegani, A. D. (2003). A systematic experimental approach to cross-flow fan design, *Transaction of the ASME Journal of Fluids Engineering, Vol. 125, July, 684, 693* .

Lighthill, M. J. (1952). On sound generated aerodynamically, i. general theory, *Proceedings of the Royal Society of London* A211: 564–587.

Lighthill, M. J. (1954). On sound generated aerodynamically, ii. turbulence as a source of sound, *Proceedings of the Royal Society of London* A222: 1–32.

Lynam, E. & Webb., H. (1919). The emission of sound by airscrews., *R. & M., No. 624* .

Maaloum, A., Kouidri, S. & Rey, R. (2004). Aeroacoustic performances evaluation of axial fans based on the unsteady pressure field on the blades surface, *Applied Acoustics* 65: 367–384.

Meakhail, T. (2005). A study of impeller-diffuser-volute interaction in a centrifugal fan, *Transaction of the ASME Journal of Turbomachinery, Vol.127, Jan., 84-90* .

Menter, F. (1993). Zonal two equation $k - \omega$ turbulence models for aerodynamic flows, *AIAA Paper* 93-2906.

Moon, Y.-J., Cho, Y. & Nam, H.-S. (2003). Computation of unsteady viscous flow and aeroacoustic noise of cross flow fans, *Computers & Fluids, Vol. 32, 995-1015* .

Moon, Y. & Seo, H. J. (2006). Linearized perturbed compressible equations for low mach number aeroacoustics., *Comput. Phys.* 218(2): 702–719.

Nogueira, X., Cueto-Felgueroso, L., Colominas, I., Khelladi, S., Navarrina, F. & Casteleiro, M. (2010). Resolution of computational aeroacoustics problem on unstructured grids with high-order finite volume scheme, *Journal of Computational and Applied Mathematics* 234 (7): 2089–2097.

Schleer, M. & Hong, S. (2004). Investigation of an inversely designed centrifugal compressor stage - part ii: Experimental investigation, *Journal of Turbomachinery* 126: 82–90.

Seo, S., Kim, K. & Kang, S. (2003). Calculations of three-dimentional viscous flow in a multiblade centrifugal fan by modeling blade forces, *Journal of Power and Energy* 217: 287–297.

Tam, C. & Webb, J. (1993). Dispersion-relation-preserving finite difference schemes for computational aeroacoustics, *J. Comput. Phys.* 107: 262–281.

Toffolo, A. (2004). On cross-flow fan theoretical performance and efficiency curves: An energy loss analysis on experimental data, *Transaction of the ASME Journal of Fluids Engineering, Vol. 126, Sept., 743-751* .

Zangeneh, M. & Schleer, M. (2004). Investigation of an inversely designed centrifugal compressor stage - part i: Design and numerical verification, *Journal of Turbomachinery* 126: 73–81.

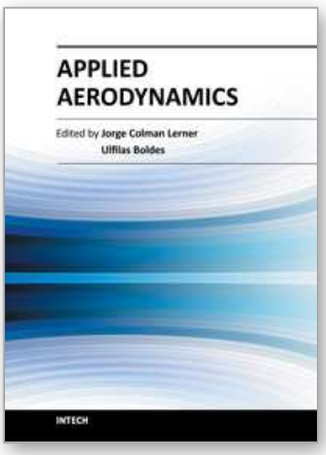

Applied Aerodynamics

Edited by Dr. Jorge Colman Lerner

ISBN 978-953-51-0611-1

Hard cover, 192 pages

Publisher InTech

Published online 11, May, 2012

Published in print edition May, 2012

Aerodynamics, from a modern point of view, is a branch of physics that study physical laws and their applications, regarding the displacement of a body into a fluid, such concept could be applied to any body moving in a fluid at rest or any fluid moving around a body at rest. This Book covers a small part of the numerous cases of stationary and non stationary aerodynamics; wave generation and propagation; wind energy; flow control techniques and, also, sports aerodynamics. It's not an undergraduate text but is thought to be useful for those teachers and/or researchers which work in the several branches of applied aerodynamics and/or applied fluid dynamics, from experiments procedures to computational methods.

INTECH
open science | open minds

InTech Europe
University Campus STeP Ri
Slavka Krautzeka 83/A
51000 Rijeka, Croatia
Phone: +385 (51) 770 447
Fax: +385 (51) 686 166
www.intechopen.com

InTech China
Unit 405, Office Block, Hotel Equatorial Shanghai
No.65, Yan An Road (West), Shanghai, 200040, China
中国上海市延安西路65号上海国际贵都大饭店办公楼405单元
Phone: +86-21-62489820
Fax: +86-21-62489821

IntechOpen